**Appendix X. Ocean Ecosystems Sensitivity Analyses and Measurement Requirements**

The appendix has four sections on remotely sensed optical, biological, and biogeochemical parameters related to the science questions, atmospheric correction sensitivity to noise, bio-optical algorithm sensitivity to noise, and a summary of ocean radiometer measurement requirements. The atmospheric correction analysis was conducted by Menghua Wang (NOAA/NESDIS) and Howard Gordon (U. of Miami). The bio-optical algorithm study was conducted by Stephane Maritorena (UC/Santa Barbara) using inputs from the Wang and Gordon study.

**Remotely Sensed Ocean Optical, Biological, and Biogeochemical Parameters**

Associated with each of the science questions is a set of geophysical parameters that must be measured in order to address the question. Remote sensing retrievals for each of these parameters requires an algorithm that transforms the basic water-leaving radiances or remote sensing reflectances into an estimated value of that parameter over a range of values. In Table 1 on the following 6 pages, the various desired geophysical parameters are shown in the left-most column. For each parameter, the second and third columns indicate baseline and threshold ranges for the parameter, respectively. Here, the 'baseline' range represents the full desired retrieval range for a given parameter and is the range of values between the 1% and 99% region for the parameter frequency distribution. The 'threshold' range is the required retrieval range for a given parameter and represents the 5% to 95% region of the frequency distribution. Baseline and threshold values for the geophysical parameters defined in Table 1 were based on analyses of both field and historical satellite measurements. Specific information regarding these analyses for each parameter is provided in the right-most column of comments. It should be noted that values for each parameter have been measured that exceed even the baseline range, but these values are found under extreme and rare conditions and were not viewed as critical retrieval requirements for a satellite mission focused on global ocean properties. Importantly, the range of parameter values shown in Table 1 places specific requirements on ACE satellite radiometry regarding spectral bands, spectral ranges, and data quality from the sensor (e.g., signal-to-noise ratio and radiometric accuracy), as well as requiring algorithm development and algorithm sensitivity analyses.

---

**Table 1.** ACE ocean geophysical parameters, retrieval baseline ranges, and retrieval threshold ranges. See comments in right-most column regarding data sets and other notes on parameter ranges.

| Geophysical Parameter | Baseline Range | Threshold Range | Comments |
|---|---|---|---|
| **Remote sensing reflectance (Rrs)** | $Rrs(340)$ 0.0015 - 0.020 $sr^{-1}$<br>$Rrs(380)$ 0.0017 - 0.020 $sr^{-1}$<br>$Rrs(412)$ 0.0011 - 0.033 $sr^{-1}$<br>$Rrs(443)$ 0.0016 - 0.024 $sr^{-1}$<br>$Rrs(490)$ 0.0023 - 0.014 $sr^{-1}$<br>$Rrs(510)$ 0.0026 - 0.011 $sr^{-1}$<br>$Rrs(531)$ 0.0021 - 0.010 $sr^{-1}$<br>$Rrs(547)$ 0.0014 - 0.009 $sr^{-1}$<br>$Rrs(555)$ 0.0014 - 0.008 $sr^{-1}$<br>$Rrs(670)$ 0.0000 - 0.002 $sr^{-1}$<br>$Rrs(678)$ 0.0000 - 0.002 $sr^{-1}$<br>$Rrs(683)$ 0.0000 - 0.012 $sr^{-1}$ | $Rrs(340)$ 0.0020 - 0.015 $sr^{-1}$<br>$Rrs(380)$ 0.0030 - 0.017 $sr^{-1}$<br>$Rrs(412)$ 0.0035 - 0.028 $sr^{-1}$<br>$Rrs(443)$ 0.0038 - 0.021 $sr^{-1}$<br>$Rrs(490)$ 0.0042 - 0.012 $sr^{-1}$<br>$Rrs(510)$ 0.0036 - 0.008 $sr^{-1}$<br>$Rrs(531)$ 0.0027 - 0.006 $sr^{-1}$<br>$Rrs(547)$ 0.0019 - 0.005 $sr^{-1}$<br>$Rrs(555)$ 0.0018 - 0.005 $sr^{-1}$<br>$Rrs(670)$ 0.0001 - 0.001 $sr^{-1}$<br>$Rrs(678)$ 0.0001 - 0.001 $sr^{-1}$<br>$Rrs(683)$ 0.0000 - 0.001 $sr^{-1}$ | Ranges in the 412-678 nm region are based on the SeaWiFS and MODIS-AQUA data. Ranges at 340, 380 and 683 nm are based on field measurements from a variety of oceanic and coastal stations (n > 1,000) extracted from the NASA SeaBASS archive. |
| **Inherent optical properties**<br>*Absorption coefficients*<br>- total absorption (a) | $a(412)$ 0.020 - 2.0 $m^{-1}$<br>$a(443)$ 0.020 - 1.8 $m^{-1}$<br>$a(555)$ 0.065 - 1.5 $m^{-1}$<br>$a(676)$ 0.460 - 1.8 $m^{-1}$ | $a(412)$ 0.03 - 0.8 $m^{-1}$<br>$a(443)$ 0.03 - 0.7 $m^{-1}$<br>$a(555)$ 0.08 - 0.6 $m^{-1}$<br>$a(676)$ 0.47 - 0.8 $m^{-1}$ | For total a and c, 1% and 5% values were based on OSU data base (450 near surface data points), 95% values based on data from the Philippines (PHILEX, two cruises), and the 99% values based on coastal OASIS observations. The $a_p$, $a_d$, and $a_{CDOM}$ values are based on NOMAD data (Mannino et al 2008, Nelson et al 2010). BIOSOPE data from the ultra-oligotrophic South Pacific gyre were used in assessing lower limits of baseline ranges (Huot et al., 2008; Bricaud et al., 2010). |
| - phytoplankton absorption ($a_{ph}$)<br>- detrital absorption ($a_d$)<br>- colored dissolved organic material absorption ($a_{CDOM}$) | $a_{ph}(443)$ 0.003 - 1.2 $m^{-1}$<br>$a_d(443)$ 0.0004 - 0.6 $m^{-1}$<br>$a_{CDOM}(443)$ 0.002 - 0.9 $m^{-1}$ | $a_{ph}(443)$ 0.007 - 0.7 $m^{-1}$<br>$a_d(443)$ 0.001 - 0.3 $m^{-1}$<br>$a_{CDOM}(443)$ 0.003 - 0.5 $m^{-1}$ | |
| *Backscatter coefficient (bb)* | $b_{bp}(443)$ 0.0003 - 0.1 $m^{-1}$ | $b_{bp}(443)$ 0.001 - 0.003 $m^{-1}$ | bbp(443) values are based on the GSM (Maritorena et al. 2002) and QAA (Lee et al 2002) inversion models applied to MODIS L3 data, |
| *Beam attenuation (c)* | $c(412)$ 0.03 - 10.0 $m^{-1}$<br>$c(443)$ 0.03 - 10.0 $m^{-1}$<br>$c(555)$ 0.08 - 10.0 $m^{-1}$ | $c(412)$ 0.1 - 0.5 $m^{-1}$<br>$c(443)$ 0.1 - 0.5 $m^{-1}$<br>$c(555)$ 0.1 - 0.5 $m^{-1}$ | |

| Parameter | | | |
|---|---|---|---|
| | c(676) 0.47 - 10.4 m⁻¹ | c(676) 0.5 - 0.9 m⁻¹ | in addition to a subset of field measurements available in SeaBASS. Coastal, sediment-dominated waters have values well beyond the stated maximum.<br><br>$a_{CDOM}$ values are based on field data which contain sampling bias in coastal regions. Recommended maxima based on satellite data and field measurements from high CDOM areas (coastal & river plumes) are 3 m⁻¹ for threshold and 10 m⁻¹ for baseline. |
| **Diffuse attenuation coefficient for downwelling plane irradiance at 490 nm [Kd(490)]** | Kd(490) 0.02 - 4.0 m⁻¹ | Kd(490) 0.02 - 1.5 m⁻¹ | Based on >6,100 in-water profiles, spanning the clearest waters (South Pacific gyre, Arctic ice zone) to very turbid and shallow riverine waters. Values are based on data in the near-surface extrapolation interval--they are not "bulk" values (Morel et al. 2007). Kd can also be derived for other wavelengths. |
| **Incident Photosynthetically Available Radiation (PAR)**<br>*Instantaneous*<br><br>*24-hr flux* | 0 - 2,200 µmol quanta m⁻² s⁻¹<br><br>0 - 60 mol quanta m⁻² d⁻¹ | 100 - 2,100 µmol quanta m⁻² s⁻¹<br><br>10 - 55 mol quanta m⁻² d⁻¹ | In some partly cloudy situations, the upper values for instantaneous PAR can be 10-15% higher due to reflection by the side of clouds.<br><br>Ranges for 24 hr PAR data based on 2004 MODIS data corrected for cloudiness and available at: oceancolor.gsfc.nasa.gov/ |
| **1% PAR depth** ($Z_{1\%}$) | 10 – 150 m | 35 – 135 m | Ranges are based on 2008 MODIS Rrs retrievals, with the 1%PAR depth calculated following Lee et al. (2007). |

| Parameter | | | Description |
|---|---|---|---|
| **Particulate inorganic carbon concentration (PIC)** | $1.2 * 10^{-5}$ - $5.3 * 10^{-4}$ mol m$^{-3}$ | $1.9 * 10^{-5}$ - $3.3 * 10^{-4}$ mol m$^{-3}$ | Values based on Atlantic Meridional Transect cruises (covering the oligotrophic gyres to eutrophic waters). N=481. Samples processed by first filtering seawater onto 0.4um polycarbonate filters and subsequently rinsed with potassium tetraborate (pH8), to rinse away seawater calcium. PIC derived from particulate calcium measurement using inductively-coupled plasma optical emission spectroscopy. Samples corrected for seawater calcium by also measuring the sodium line with the ICP-OES. Statistics calculated on log transformed data. |
| **Particulate Organic Carbon concentration (POC)** | 15 - 2,000 mg m$^{-3}$ | 20 - 500 mg m$^{-3}$ | Values based on 804 field measurements from ultra-oligotrophic to turbid coastal environments. Minimum and maximum surface values of POC derived from both field and satellite data are about 10 mg m$^{-3}$ and 10,000 mg m$^{-3}$. In extreme cases values in excess of 10,000 mg m$^{-3}$ have been observed |
| **Dissolved Organic Carbon concentration (DOC)** | 35-800 µmol L$^{-1}$ | 40-500 µmol L$^{-1}$ | Values based on field data. Surface DOC in the field ranges from 35 to 1,000 µmol L$^{-1}$. Typical river plume DOC is 650 umol L$^{-1}$ for Arctic and tropical rivers, but DOC can exceed 1,000 µmol L$^{-1}$. |
| **Suspended Particulate Matter concentration (SPM)** | 25 - 70,000 mg m$^{-3}$ | 45 - 15,000 mg m$^{-3}$ | Values based on 271 field measurements from ultra-oligotrophic to turbid coastal |

| Parameter | Baseline | Threshold | Comments |
|---|---|---|---|
| | | | environments. For this data set, the minimum SPM = 22 mg m⁻³ and the maximum ~140,000 mg m⁻³. In some aquatic environments higher values can be observed. |
| **Particle size characteristics** (size ranges indicted here) | 0.05 - 2,000 $\mu$m | 0.8 - 200 $\mu$m | Threshold values reflect current measurement capabilities for seawater samples using electronic counting/sizing (e.g., Coulter) and laser diffraction (e.g., LISST). Baseline values represent a desired, environmentally-relevant range requiring near-term instrument/technique development. |
| **Total Chlorophyll-a concentration** ($C_{phyto}$) | 0.015 - 40 mg m⁻³ | 0.030 - 25 mg m⁻³ | Values based on field and satellite (SeaWiFS) data. Field data are from SeaBASS and include HPLC and Turner fluorescence measurements. |
| **Other phytoplankton pigments** | To be defined | To be defined | |
| **Phytoplankton Carbon concentration** ($C_{phyto}$) | 0.15 - 800 mg m⁻³ | 3.0 - 450 mg m⁻³ | Values based on satellite retrievals of $b_{bp}$ converted to $C_{phyto}$ following Westberry et al. (2008). |
| **Normalized Fluorescence Line-height** (FLH) | 0.0001 - 0.025 mW cm⁻² $\mu$m⁻¹ sr⁻¹ | 0.001 - 0.015 mW cm⁻² $\mu$m⁻¹ sr⁻¹ | Values based primarily on MODIS L3 data, but in situ data (NOMAD) were also used for evaluating maximum criteria |
| **Fluorescence Quantum Yield** (FQY) | 0.0003 - 0.05 fluoresced photons (absorbed photons)⁻¹ | 0.001 - 0.02 fluoresced photons (absorbed photons)⁻¹ | Values based on MODIS L3 data following Behrenfeld et al. (2009), which includes a correction for non-photochemical quenching that reduces FQY values at low-light |

| Parameter | | | |
|---|---|---|---|
| **Net Primary Production** (NPP) | 55 - 8,500 mg m$^{-2}$ d$^{-1}$ | 90 - 4,500 mg m$^{-2}$ d$^{-1}$ | Values based on field and satellite (SeaWiFS) data. Satellite data are from the VGPM (Behrenfeld & Falkowski 1997). Field data are from the OSU productivity website: www.science.oregonstate.edu/ocean.productivity/ |
| **Phytoplankton physiological properties** | | | Growth rate values based on satellite Chl:C data, light attenuation, and mixing depth (Westberry et al. 2008). |
| *Chl:C* | 0.0005 - 0.3 mg mg$^{-1}$ | 0.001 - 0.1 mg mg$^{-1}$ | |
| *Growth Rate* | 0.00 - 1.9 d$^{-1}$ | 0.01 - 1.5 d$^{-1}$ | |
| **Phytoplankton groups** | | | Size-based groups from exclusively open-ocean field HPLC- pigment data (Uitz et al. 2006), with a baseline surface chlorophyll-a range of 0.03 - 5.8 mg m$^{-3}$. Only data from the first optical depth are included. See Uitz et al. (2006) for details. Alternative approaches for defining phytoplankton groups are also under investigation. |
| *Size-based groups expressed as a fraction of total algal chlorophyll* | microphytoplankton: 0 - 0.9 nanophytoplankton: 0 - 0.9 picophytoplankton: 0 - 1.0 | microphytoplankton: 0 - 0.7 nanophytoplankton: 0.2 - 0.8 picophytoplankton: 0 - 0.8 | |
| *Trichodesmium concentration* | 0 – 10,000 filaments L$^{-1}$ | 0 – 5,000 filaments L$^{-1}$ | Values based on ~20 years of field data (largely epifluorescence microscopy of filtered seawater). When necessary, filaments L$^{-1}$ was estimated assuming 200 filaments colony$^{-1}$ (Carpenter, 1983). A large bloom can exceed 10$^6$ filaments L$^{-1}$. |
| *Coccolith concentration* | 293 - 814,930 detached coccoliths mL$^{-1}$<br><br>34 - 3,624 plated | 760 - 314,000 detached coccoliths mL$^{-1}$<br><br>59 - 2,066 plated | Values based on field data from Atlantic Meridional Transect cruise 17 (n=412 samples) which included oligotrophic to temperate waters and a coccolithophore bloom |

| coccolithophores per coccolith aggregates mL$^{-1}$ | coccolithophores per coccolith aggregates mL$^{-1}$ | Statistics calculated on log transformed data. Note, highest published concentrations of detached coccoliths in the field are ~500,000 mL$^{-1}$. The baseline upper range of 800,000 mL$^{-1}$ (statistically defined here by the upper 99th percentile of log-normal variance), thus, appears high. Plated coccolithophores are combined with coccolith aggregates because discrimination is difficult when using birefringence microscopy. |
|---|---|---|
| | | |

*References for Table 1*

 Behrenfeld, M.J. & P.G. Falkowski. 1997. Photosynthetic rates derived from satellite-based chlorophyll concentration. Limnol. Oceanogr. 42:1-20

Behrenfeld, M.J., et al. (2009), Satellite-detected fluorescence reveals global physiology of ocean phytoplankton, Biogeosciences v6, 779-794.

Bricaud, A., M. Babin, H. Claustre, J. Ras, and F. Tièche (2010), Light absorption properties and absorption budget of Southeast Pacific waters, J. Geophys. Res., 115, C08009, doi:10.1029/2009JC005517.

Carpenter, E. J. (1983), Nitrogen fixation by marine Oscillatoria (Trichodesmium) in the world's oceans, in Nitrogen in the Marine Environment, edited by E. J. Carpenter and D. G. Capone, pp. 65– 103, Elsevier, New York.

Huot, Y., A. Morel, M. S. Twardowski, D. Stramski, and R. A. Reynolds (2008), Particle optical scattering along a chlorophyll gradient in the uper layer of the eastern South Pacific Ocean. Biogeosciences, 5, 495-507.

Lee, Z. P., K. L. Carder, and R. Arnone (2002), Deriving inherent optical properties from water color: A multi-band quasi-analytical algorithm for optically deep waters, Applied Optics, 41, 5755-5772.

Lee, Z. P., A. Weidemann, J. Kindle, R. Arnone, K. L. Carder, and C. Davis (2007), Euphotic zone depth: Its derivation and implication to ocean-color remote sensing, J. Geophys. Res., 112, C03009, doi:03010.01029/02006JC003802.

Mannino, A., M.E. Russ, and S.B. Hooker, (2008), Algorithm development and validation for satellite-derived distributions of DOC and CDOM in the US Middle Atlantic Bight. J. Geophys. Res., 113: C07051.

Maritorena S., D.A. Siegel & A. Peterson. 2002. Optimization of a Semi-Analytical Ocean Color Model for Global Scale Applications. *Applied Optics*. 41(15): 2705-2714.

Morel, A., Y. Huot, B. Gentili, P.J. Werdell, S.B. Hooker, and B. Franz, 2007: Examining the consistency of products derived from various ocean color sensors in open ocean (Case 1) waters in the perspective of a multi-sensor approach. Remote Sens. Environ., 111, 69-88.

Nelson, N. B., D. A. Siegel, C. A. Carlson, and C. M. Swan (2010), Tracing global biogeochemical cycles and meridional overturning circulation using chromophoric dissolved organic matter, Geophys. Res. Lett., 37, L03610, doi:10.1029/2009GL04232.

Uitz, J., H. Claustre, A. Morel, and S. B. Hooker (2006), Vertical distribution of phytoplankton communities in open ocean: An assessment based on surface chlorophyll, J. Geophys. Res., 111, C08005, doi: 10.1029/2005JC003207.

T. Westberry, M.J. Behrenfeld, D.A. Siegel, E. Boss. 2008. Carbon-based primary productivity modeling with vertically resolved photoacclimation. ***Global Biogeochem. Cycles***. 22, GB2024, doi:10.1029/2007GB003078

**Simulations for the NIR and SWIR SNR Requirements for Atmospheric Corrections**

Atmospheric correction for ocean color product is extremely sensitive to sensor spectral band calibration errors, as well as to radiometric noise. This is due to the considerably low radiance from the ocean compared to the sensor-measured top-of-atmosphere (TOA) radiance. The sensor spectral band radiometric performance can be characterized by the signal to noise ratio (SNR). To understand the radiometric noise effects on the derived normalized water-leaving reflectance spectra, simulations of atmospheric correction, using the two near-infrared (NIR) bands (765 and 865 nm) and various combinations of the shortwave infrared (SWIR) bands (1240, 1640, and 2130 nm), have been carried out for several levels of sensor noise.
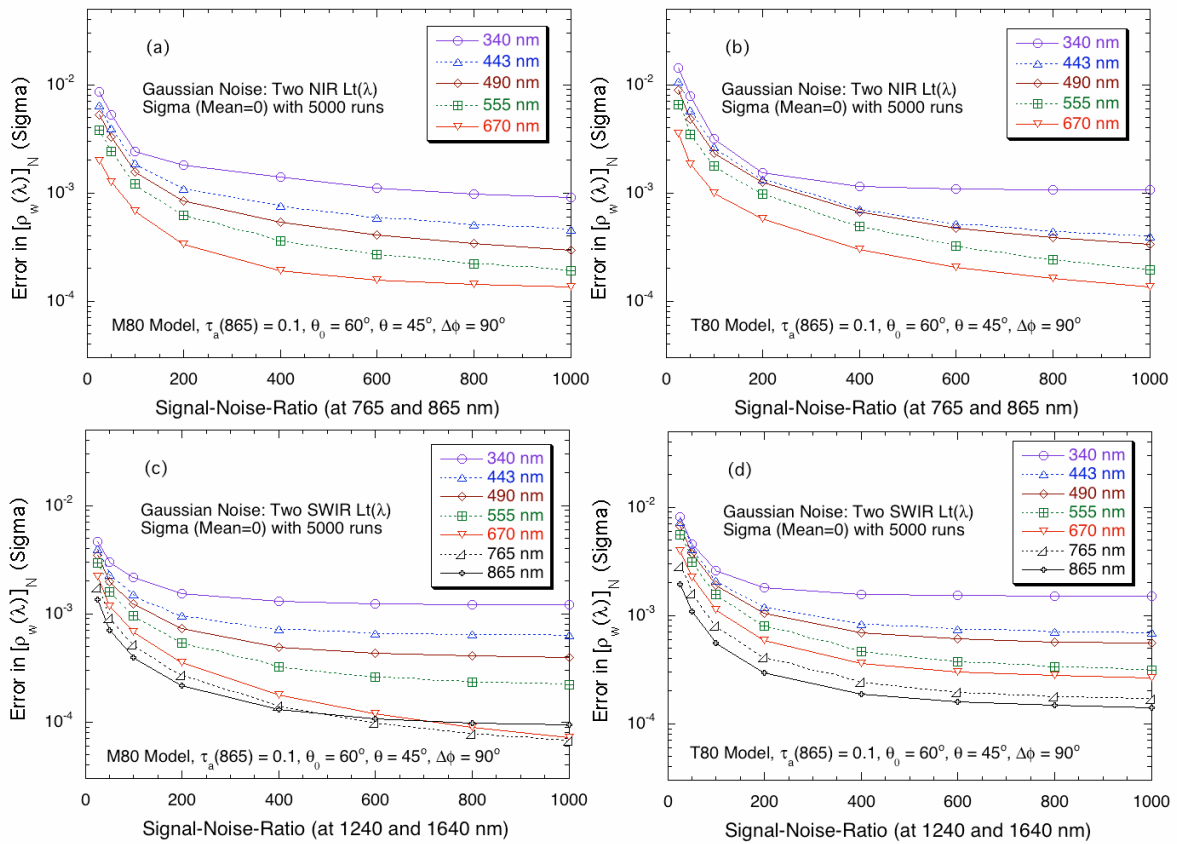
*Noise Model*. A Gaussian distribution (with mean value = 0) is used for the noise simulations. The standard deviation (STD) of the Gaussian distribution is the radiance noise level (i.e., related to the SNR values). The simulated reflectance noise is then added into the TOA reflectance at various NIR and SWIR bands that are used for making atmospheric correction. Eight noise levels are generated, corresponding to eight SNR values of 25, 50, 100, 200, 400, 600, 800, and 1000. It is noted that the reflectance noise is only added into the bands that are used for atmospheric correction (e.g., two NIR bands), and UV and visible bands are noise free in all simulations discussed in this subsection. The reflectance noises are spectrally incoherent.

*Atmospheric Correction*. Atmospheric correction simulations using two NIR bands (Gordon and Wang, 1994) and various SWIR bands (Wang, 2007) have been carried out including reflectance noise levels for the corresponding NIR and SWIR bands. Specifically, simulations were carried out for a typical Maritime aerosol model (M80) and a Tropospheric model (T80), where the T80 model is actually M80 model without the large size fraction, for aerosol optical thicknesses (at 865 nm) of 0.05, 0.1, 0.2, and 0.3. The M80 and T80 aerosol models were not used in the aerosol lookup tables for atmospheric correction (Gordon and Wang, 1994; Wang, 2007). Simulations were performed for a case with solar-zenith angle of 60°, sensor-zenith angle of 45°, and relative azimuth angle of 90°.
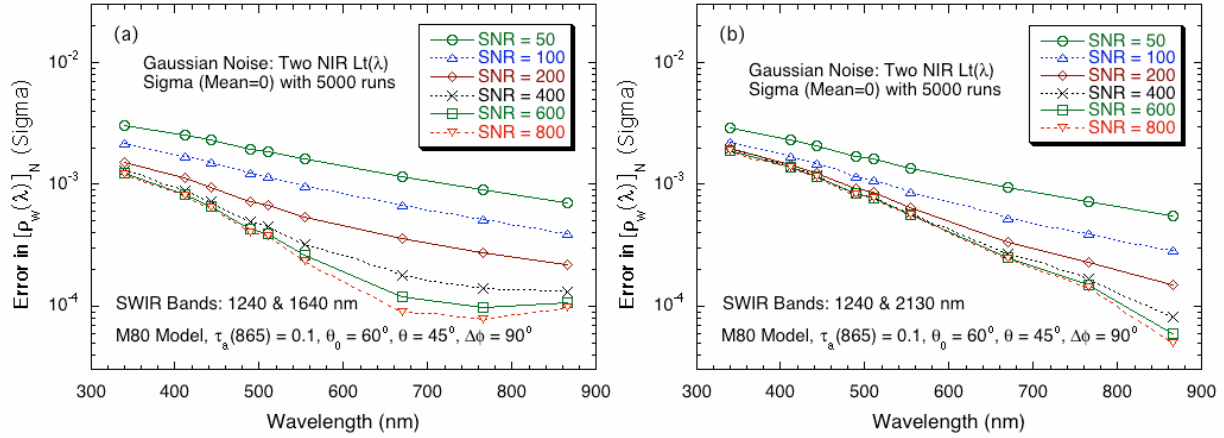
*SNR Simulations*. For each case, atmospheric correction for 5000 noise realizations with a given SNR value was carried out. For example, for a case with aerosol optical thickness (AOT) at 865 nm of 0.1, 5000 reflectance noise samples (with a given SNR value) were generated and added into the TOA NIR (765 and 865 nm) reflectance values. The NIR atmospheric correction (Gordon and Wang, 1994) was then performed 5000 times to generate the corresponding normalized water-leaving reflectance spectra error. The same procedure was carried out for all four AOTs and also for the SWIR algorithm (Wang, 2007). In the SWIR atmospheric correction, however, the Gaussian noise was of course added into the SWIR bands (error free for UV to NIR bands). This produces the uncertainty in the derived normalized water-leaving reflectance from the UV to the red (or NIR in the case of the SWIR bands). In effect, the simulated uncertainty includes errors from both the atmospheric correction algorithm and the added Gaussian noise in the NIR or SWIR bands. The reflectance uncertainty spectra (from UV to red) are then used for the bio-optical model sensitivity analysis by Stephane Maritorena.

*Example Results*. Figure 1 provides sample results in the reflectance uncertainty spectra (UV to red or UV to NIR) with simulations from atmospheric correction algorithm using the NIR or SWIR bands. The error in the normalized water-leaving reflectance, $[\rho_w(\lambda)]_N$, is actually the standard deviation of the derived uncertainty in $[\rho_w(\lambda)]_N$ over the 5000 Gaussian noise realizations, i.e., each point in the plot was derived from 5000 simulations ($[\rho_w(\lambda)]_N$ errors were

first obtained with these 5000 simulations and then STD error was derived).  The STD error was computed assuming that the mean value = 0 (i.e., error free).  Figures 1(a) and 1(b) are results for the NIR atmospheric correction algorithm (using 765 and 865 nm) with the M80 and T80 aerosol models, respectively, while Figures 1(c) and 1(d) are results for the M80 and T80 aerosols using the SWIR atmospheric correction algorithm (with bands of 1240 and 1640 nm) for various SNR values.  Note that for the SWIR results (Figures 1(c) and 1(d)), errors in $[\rho_w(\lambda)]_N$ for two NIR bands are also included.  Results in Figure 1 show that, as SNR value increases (or noise decreases), error in $[\rho_w(\lambda)]_N$ decreases (as expected), and it reaches the inherent algorithm error (Gordon and Wang, 1994; Wang, 2007).



**Figure 1.**  Error in the derived normalized water-leaving reflectance (in standard deviation with the mean value of 0) from 5000 Gaussian noise realizations as a function of the SNR value using the NIR (plots a and b) and SWIR (plots c and d) atmospheric correction algorithms. Aerosol model and AOT value, as well as solar-sensor geometry are indicated in each plot.  For the NIR algorithm, error spectra data from UV to red are provided (plots a and b), while for the SWIR algorithm error spectra from UV to NIR are shown (plots c and d).

**Figure 2.** Error in the derived normalized water-leaving reflectance (in standard deviation with the mean value of 0) from 5000 Gaussian noise realizations as a function of the wavelength for various SNR values using the SWIR atmospheric correction algorithm with two SWIR bands of (a) 1240 and 1640 nm and (b) 1240 and 2130 nm. Aerosol model and AOT value, as well as solar-sensor geometry are indicated in each plot.

Figure 2 provides sample results in the reflectance uncertainty spectra as a function of the wavelength (UV to NIR) for various SNR values with simulations from atmospheric correction algorithm using the two SWIR band sets, i.e., 1240 and 1640 nm (Figure 2(a)) and 1240 and 2130 nm (Figure 2(b)). Importantly, results in Figure 2 show that errors in $[\rho_w(\lambda)]_N$ from atmospheric correction are spectrally coherent. In addition, Figure 2 demonstrates that a SNR value between ~200-300 for the SWIR bands 1240 and 1640 nm is adequate (Figure 2(a)), while for the SWIR band 2130 nm a minimum of SNR value ~100 is required. At these SNR values for the SWIR bands, the derived water-leaving reflectance spectra from the SWIR atmospheric correction algorithms almost reach their corresponding algorithm inherent accuracy. It should be noted that, however, with even higher SNR values the derived $[\rho_w(\lambda)]_N$ at the red and NIR bands can be further improved.

*Summary.* Atmospheric correction and bio-optical simulations (see results from Stephane Maritorena) suggest that (1) for the NIR bands a minimum SNR value of ~600 is required, and (2) for the SWIR bands at 1240 and 1640 nm a minimum SNR value of ~200-300 is required, while for the 2130 nm band a minimum SNR value of ~100 is adequate.

**Bio-optical model sensitivity analysis**

Simulations were performed to assess how noise in the spectral marine remote sensing reflectance, Rrs(λ), affects the retrievals of biogeochemical variables from a semi-analytical ocean color model (GSM01, Maritorena et al., 2002). These analyses were performed in order to assess the required SNRs in the ACE visible bands to ensure accurate bio-optical retrievals. Noise is created from the at-sea-level atmosphere reflectance spectra derived from the atmosphere specific simulations ran by Menghua Wang. The spectral atmospheric noise is added to a marine reflectance spectrum at the surface derived from a chlorophyll-based model (Morel

and Maritorena, 2001). We compared the model retrievals obtained when spectral reflectance is contaminated by noise to those retrieved from noise-free spectra. These simulations were run for a variety of atmospheric and marine conditions. This is briefly described below.

Two main kinds of noise were considered: 1) Atmospheric noise caused by errors in the NIR bands and propagated to the visible bands and, 2) noise as a random, spectrally uncoherent fraction of the Top-of-Atmosphere (TOA) reflectance in addition to the NIR created noise. This latter case was designed to represent radiometric noise from other sources than the NIR bands (e.g. calibration). These two cases, will be referred to as "NIR" and "radiometric" errors, respectively.

In all runs, the "pure" marine Rrs signal ( = no noise) is generated from the MM01 model (Morel & Maritorena, 2001) for 10 chlorophyll concentration (CHL) values in the 0.02-5 mg/m$^3$ range (400-700 nm every 5 nm). The GSM01 retrievals from the inversion of these "no noise" spectra are the reference to which the "noisy" NIR and radiometric cases are compared to.

For the "NIR" errors case, the at-sea-level reflectance spectra caused by errors in the NIR bands (from Menghua Wang) are converted to Rrs, Rrs_NIR($\lambda$), and added to a MM01 marine spectrum, Rrs_MM01($\lambda$, CHL), so

Rrs($\lambda$, ocean) = Rrs_MM01($\lambda$, CHL)+ Rrs_NIR($\lambda$)

The resulting spectrum, Rrs($\lambda$, ocean), is then inverted in GSM. The three GSM retrievals (CHL, CDM, BBP) are then compared to the "no noise" case for 5000 spectra for each combination of SNR (8 values), AOT(865) and atmospheric model (2 models) and marine Rrs($\lambda$) (10 spectra). The comparisons are expressed in terms of the %rms for each of the GSM01 product and at each Chl level used to generate the marine Rrs. The %rms is defined as rms*100/reference (reference = retrieval in the no noise case).

For the "radiometric" errors case, a random, Gaussian, spectrally uncoherent fraction of a TOA signal is added to the marine spectra created similarly to what is described in the "NIR" case above. First, TOA signals are constructed for a black ocean with the M80 and T80 models, AOT(865) = 0.1 and for solar, sensor, and relative azimuth angles of 60, 45, and 90 degrees, respectively. The ocean contribution to the TOA signal is calculated as a MM01 reflectance spectrum transmitted through the atmosphere (with transmittance values matching the atmospheric model and geometry and AOT(865) of 0.05, 0.1, 0.2, and 0.3) and is added to the atmospheric TOA component (converted to Rrs units; Rrs_TOA($\lambda$)). The fraction of the TOA signal that is added to the marine spectrum created as in the NIR cases is determined through the generation of random Gaussian numbers with a mean of 0 and a standard-deviation of 1/SNR(visible) with SNR(visible) set to 10., 20., 40., 100., 200., 400., 800., 1000. and 2000. Then, each wavelength of the TOA spectrum is multiplied by a unique random number (rn) and that fraction of the TOA spectrum is added to the other components of the marine signal. This is done independently for each of the 5000 spectra corresponding to each SNR(NIR)/AOT(865)/atmospheric model combination used in the atmosphere simulations. In summary, in the "radiometric" errors case the at-sea-level Rrs is generated as:

Rrs($\lambda$, ocean) = Rrs_MM01($\lambda$, CHL)+ Rrs_NIR($\lambda$) + (Rrs_TOA($\lambda$) * rn($\lambda$, SNR(visible))

By looking at how much the retrievals from the noisy reflectance spectra depart from those derived without addition of noise, it is possible to assess the SNR(visible) value that allows an

acceptable accuracy in the retrievals. It should be mentioned that in this approach, we assume an identical SNR level throughout the visible spectrum and does not take into account the fluorescence bands.  Figures 3 and 4 illustrate the results of these analyses.
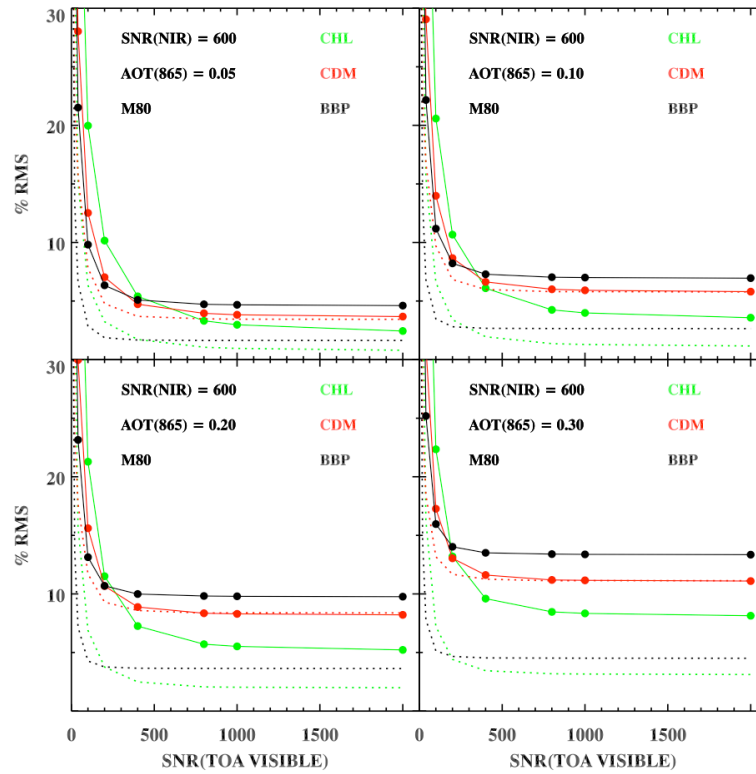


Figure 3. Example of the average (solid lines and symbols) and standard-deviation (dotted lines) of the %rms error over the full range of CHL values used as input in MM01 for the 3 GSM01 retrievals (green: CHL, red: CDM, black: BBP) as a function of the SNR values in the visible and for SNR(NIR)=600 and different AOT(865) values.
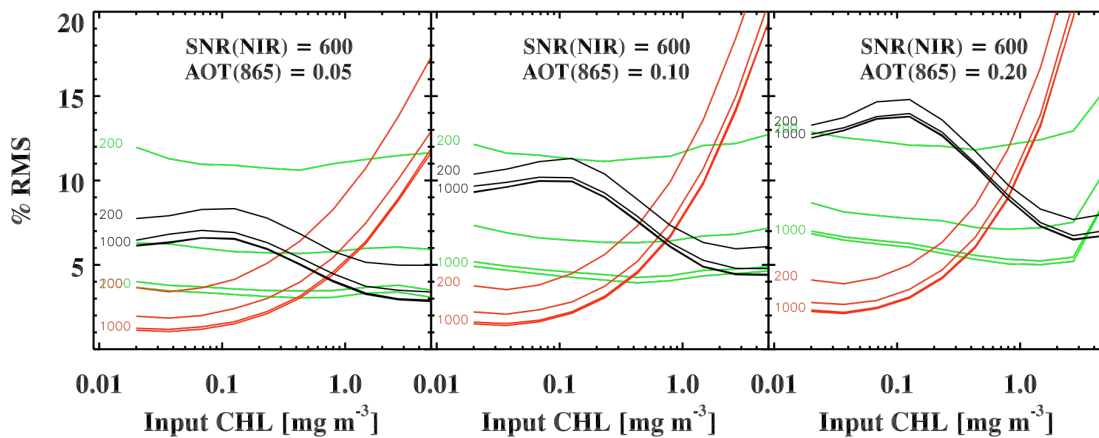


Figure 4.  Example of the %rms error for each of the GSM01 retrievals (green: CHL, red: CDM, black: BBP) as a function of the CHL values used as input in MM01 for  SNR(NIR)= 600 and different AOT(865) values. For each retrieval, the curves for SNR(visible) of 200, 400, 800 and 1000 are plotted, the highest (=1000) and lowest (=200) SNR(visible) values are indicated at

either the beginning or the end of each curve.

For the minimum SNR(NIR) value of 600 suggested above, Figure 4 shows that for the three GSM retrievals the errors become stable in the 800-1000 SNR(vis) range (CHL gets stable at higher SNRs than the other 2 retrievals). The mean error (for the full range of CHL values used as input into MM01) remains under 10% for the clear atmosphere cases only (AOT(865) ≤ 0.1). This is confirmed in Figure 3 where the errors in the GSM retrievals stay under or close to 10% (except for CDM in eutrophic waters) for clear atmospheres and high SNRs. For the visible bands, a minimum SNR of ~1000 is thus recommended.

**Measurement requirements summary**
The ocean radiometer requirements are outlined in the following two tables. The first provides general sensor performance and mission support requirements. The second lists specific data on multispectral bands, bandwidths, typical clear sky top-of-atmosphere radiances over the ocean, saturation radiances, and <u>minimum</u> SNRs (based on the analyses above). In Table 2, the SNR value at 350 nm is lower than in the other UV bands because its application for detecting absorbing aerosols does not require a value of 1000. Also, the SNR at 678 nm is set at 1400 based on analysis of MODIS retrievals (the bio-optical sensitivity analyses above did not include fluorescence line height). In the wavelength domain of 345-755 nm, multispectral bands are aggregations of 5 nm hyperspectral bands.

Table 2. General requirements for ocean radiometer and mission support.
Radiometer Spectral Attributes
- 26 multispectral bands (Table 2) including
  10 nm fluorescence bands (667, 678, 710, 748 nm band centers)
  10 to 40 nm bandwidth aerosol correction bands at 748, 765, 865, 1245, 1640, 2135 nm
  820 nm band for estimation of column water vapor concentration
  350 nm band for absorbing aerosol detection
- 5 nm resolution 345 to 755 nm (functional group derivative analyses)
- Polarization: < 1.0% sensor radiometric sensitivity, 0.2% prelaunch characterization accuracy
- No saturation in multispectral bands

Accuracy and Stability
- < 2% prelaunch radiance calibration accuracy
- On-orbit vicarious calibration accuracy to 0.2%
- 0.1% radiometric stability knowledge (mission duration)
- 0.1% radiometric stability (1 month prelaunch verification)

Spatial Coverage
- Two day global coverage (58.3$^{\circ}$ cross track scanning)
- 1 km resolution at center of swath

Other
- Sensor tilt (±20$^{\circ}$) for glint avoidance
- 5 year minimum design lifetime
- Monthly lunar imaging at 7° phase angle through Earth-view sensor port

Table 3. OES multispectral band centers, bandwidths, typical top-of-atmosphere clear sky ocean radiances (Ltyp), saturation radiances (Lmax), and <u>minimum</u> SNRs at Ltyp. Radiance units are mW/cm$^2$ μm str.

### References

| λ | ∇λ | Ltyp | Lmax | SNR-spec |
|---|---|---|---|---|
| 350 | 15 | 7,46 | 35.6 | 300 |
| 360 | 15 | 7.22 | 37.6 | 1000 |
| 385 | 15 | 6.11 | 38.1 | 1000 |
| 412 | 15 | 7.86 | 60.2 | 1000 |
| 425 | 15 | 6.95 | 58.5 | 1000 |
| 443 | 15 | 7.02 | 66.4 | 1000 |
| 460 | 15 | 6.83 | 72.4 | 1000 |
| 475 | 15 | 6.19 | 72.2 | 1000 |
| 490 | 15 | 5.31 | 68.6 | 1000 |
| 510 | 15 | 4.58 | 66.3 | 1000 |
| 532 | 15 | 3.92 | 65.1 | 1000 |
| 555 | 15 | 3.39 | 64.3 | 1000 |
| 583 | 15 | 2.81 | 62.4 | 1000 |
| 617 | 15 | 2.19 | 58.2 | 1000 |
| 640 | 10 | 1.90 | 56.4 | 1000 |
| 655 | 15 | 1.67 | 53.5 | 1000 |
| 665 | 10 | 1.60 | 53.6 | 1000 |
| 678 | 10 | 1.45 | 51.9 | 1400 |
| 710 | 15 | 1.19 | 48.9 | 1000 |
| 748 | 10 | 0.93 | 44.7 | 600 |
| 765 | 40 | 0.83 | 43.0 | 600 |
| 820 | 15 | 0.59 | 39.3 | 600 |
| 865 | 40 | 0.45 | 33.3 | 600 |
| 1245 | 20 | 0.088 | 15.8 | 250 |
| 1640 | 40 | 0.029 | 8.2 | 180 |
| 2135 | 50 | 0.008 | 2.2 | 100 |

Gordon, H. R. and M. Wang, Retrieval of water-leaving radiance and aerosol optical thickness over the oceans with SeaWiFS: A preliminary algorithm, *Appl. Opt.*, 33, 443-452, 1994.

Maritorena, S., D.A. Siegel and A. Peterson, Optimization of a Semi-Analytical Ocean Color Model for Global Scale Applications. *Applied Optics*. 41:15, 2705-2714, 2002.

Morel A. and S. Maritorena, Bio-optical properties of oceanic waters : a reappraisal. *J. Geophys. Res.*, 106:C4, 7163-7180, 2001.

Wang, M., Remote sensing of the ocean contributions from ultraviolet to near-infrared using the shortwave infrared bands: simulations, *Appl. Opt.*, 46, 1535-1547, 2007.